Title page

Epidermal nanostructures enhance thermoregulation in alpine lizards by reducing near-infrared reflectance

Zhongyi Yao[1, 2#], Wenjun Tan[1, 2#], Zhijie Cao[3#], Yuning Cao[1, 2, 4], Jiajia Yin[5], Heng Shi[6], Jinzhao Ke[1, 2, 7], Jun Tao[1, 2, 4], Chenchen Yang[1, 2], Jinzhong Fu[8], Bin Fan[5], Jingxuan Wei[3], Yin Qi[1, 2*]

[#] These authors contributed equally to this work

[*] Corresponding author: qiyin@cib.ac.cn

[1] China-Croatia Belt and Road Joint Laboratory on Biodiversity and Ecosystem Services, Chengdu Institute of Biology, Chinese Academy of Sciences, Chengdu 610213, China
[2] Mountain Ecological Restoration and Biodiversity Conservation Key Laboratory of Sichuan Province, Chengdu Institute of Biology, Chinese Academy of Sciences, Chengdu 610213, China
[3] School of Optoelectronic Science and Engineering, University of Electronic Science and Technology of China, Chengdu 611731, China
[4] University of Chinese Academy of Sciences, Beijing, China
[5] State Key Laboratory of Optical Field Manipulation Science and Technology, Institute of Optics and Electronics, Chinese Academy of Sciences, Chengdu 610209, China
[6] Institute of Optics and Electronics, Chinese Academy of Sciences, Chengdu 610209, China
[7] College of Life Sciences, Sichuan University, Chengdu, China
[8] Department of Integrative Biology, University of Guelph, Ontario, Canada

Running title: NIR anti-reflective skin nanostructures aid thermoregulation

Abstract

Ectothermic survival on the Tibetan Plateau, one of the most thermally challenging terrestrial environments, requires effective heat acquisition, yet the physiological and structural mechanisms enabling thermoregulation at high altitudes remain poorly resolved. Here, we demonstrated that high-altitude lizards warmed significantly faster than lowland relatives and showed reduced skin reflectance in both the visible and near-infrared spectra. Morphological examination identified two major adaptations: elevated melanin accumulation that reduced visible light reflectance, and thickened epidermal layers embedded with nanostructures that suppresses near-infrared reflectance through broadband anti-reflective effects consistent with effective medium theory in physical optics. As near-infrared wavelengths lie beyond the visual sensitivity of most predators, these adaptations likely represent an evolutionary strategy to amplify solar radiation uptake without increasing visual conspicuousness. These features may also reduce radiative heat loss and improve thermal insulation. This study not only identifies a previously unrecognized nanophotonic adaptation for near-infrared absorption in vertebrate skin, but also provides a functional template for the design of bioinspired thermal management materials.

Keywords: skin microstructure; near-infrared; anti-reflection; thermoregulation; high elevation; *Phrynocephalus*

Introduction

Survival in extreme environments depends on the capacity to regulate body temperature with efficiency, a requirement that profoundly influences animal physiology, behavior, and ecology (*1*, *2*). High-altitude environments impose particularly severe thermal challenges, marked by persistently low ambient temperatures and intense convective winds. In such settings, both the absorption and retention of heat are essential for survival (*3*, *4*). Common thermoregulatory strategies include increased body mass, deposition of subcutaneous fat, sun-oriented basking behavior, and shifts among microhabitats with differing thermal properties (*3*, *5–7*). While these physiological and behavioral adaptations are well documented, emerging evidence suggests the existence of additional, largely uncharacterized mechanisms that contribute to thermal balance (*8*, *9*). For ectotherms, particularly heliothermic species such as sun-basking lizards, maximizing the efficiency of solar heat absorption while minimizing surface heat loss may represent a critical determinant of fitness. To date, however, the mechanistic basis of heat acquisition and conservation in such organisms remains poorly understood.

Integumentary and optical specializations are increasingly recognized as central components of thermoregulatory function across animal taxa. Mammals and birds frequently rely on structural modifications that trap air within fur or feathers to reduce convective and radiative heat loss (*10*, *11*), but such features are absent in extant non-avian reptiles. Many species also enhance visible-light absorption through thermal melanism, thereby increasing solar heat gain at the body surface (*8*, *12*). However, far less is known about how animals exploit the near-infrared (NIR) portion of the solar spectrum, which accounts for nearly half of the solar radiation reaching the Earth's surface (*8*). Unlike visible light, NIR wavelengths lie beyond the visual range of most vertebrate predators, permitting thermoregulatory benefits without increasing conspicuousness (*8*, *13*). This decoupling of thermal absorption from detection risk makes NIR exploitation a promising but underexplored pathway for enhancing thermal performance.

Although evidence for NIR-regulating adaptations has been documented in a few taxa, including certain birds, chameleons, insects, and gastropods, ecological interpretations of these patterns are often incomplete (*2*, *14–17*). In most cases, structural modifications serve to increase NIR reflectance, presumably to prevent overheating. In contrast, adaptations that reduce NIR reflectance, thereby accelerating heat gain, are rarely documented (*16*). Where such traits exist, surface nanostructures appear to play a central role in modulating NIR optical properties. By minimizing NIR reflectance, these structures may enable more rapid solar warming, allowing earlier daily activity, extended foraging windows, and improved access to thermal or reproductive resources. Under cold, high-altitude conditions, such an enhancement in thermal efficiency could provide a strong selective advantage (*18*).

The agamid lizard genus *Phrynocephalus* provides an ideal model for exploring the evolution of functional structures under cold environmental pressure. Thirty-seven recognized species are distributed across the arid deserts and high-altitude plateaus of Asia, spanning pronounced elevational gradients (*19*, *20*). Several viviparous lineages have undergone adaptive radiation to occupy extreme high-elevation habitats, with distributions extending from approximately 4 000 m

to above 5 000 m above sea level (*21*). Along these gradients, ambient temperature declines sharply, despite relatively stable incident solar radiation, while intense winds further exacerbate heat loss at higher elevations. For diurnal, heliothermic lizards that rely on basking to elevate body temperature (*22*, *23*), these conditions impose severe thermal constraints, as the difference between preferred body temperature and environmental temperature increases with elevation (*24*). Consequently, high-elevation *Phrynocephalus* populations may have evolved specialized structures to enhance solar energy utilization and limit heat loss, thereby improving thermal performance in cold climates.

To investigate potential adaptations to high-altitude cold stress, populations from four *Phrynocephalus* species, *P. forsythii*, *P. putjatai*, *P. vlangalii*, and *P. erythrurus* were sampled across a broad elevational range (Table S1). A multilevel analytical framework was applied to connect interspecific variation in thermal performance with underlying differences in skin structure and optical properties. Heating rates were measured for each species, accounting for body size, and variation in skin reflectance, transmission, melanin content, and microstructural architecture was quantified along the altitudinal gradient. The optical behavior of epidermal nanostructures was simulated using effective medium theory (EMT), while their contribution to thermal retention was evaluated through thermodynamic modeling. This integrative approach revealed high-altitude thermoregulatory innovations in cold-adapted ectotherms (Fig. 1), offering a functional template for the design of bioinspired materials engineered for passive heat management.

Results

High-altitude lizards exhibit accelerated heating

Environmental temperature exerts strong selective pressure on diurnal ectotherms, shaping behavioral strategies for thermoregulation, such as basking orientation and microhabitat use (*22–25*). On the Tibetan Plateau, high-altitude lizards experience substantially colder ambient conditions compared to lowland populations, despite exposure to similarly intense solar radiation (Fig. 2a–c). Under such constraints, more rapid heat gain may confer a distinct advantage by reducing the time required to attain active body temperature. We therefore hypothesized that high-altitude taxa would exhibit faster heating rates as an adaptive response.

To test this hypothesis, heating rates were quantified as the time (Δt) required for individuals to warm from 15 °C to 25 °C under standardized laboratory conditions (Fig. 2d). To ensure that Δt reflected a stable physiological trait rather than transient behavioral variation or condition-dependent effects (*26*, *27*), within-individual repeatability across body regions was assessed. Correlation analyses confirmed high repeatability across measures ($p < 0.05$; Table S2), and the trunk surface exhibited strong region-specific consistency (center trunk: ICC = 0.867; lower trunk: ICC = 0.770). The average value across these two trunk regions was therefore used for subsequent comparative analyses.

No significant phylogenetic signal was detected in heating rates across the studied taxa (Blomberg's K; all $p > 0.05$; Table S3), indicating that interspecific variation was not constrained by shared evolutionary history. Critically, after controlling for body size, sex, and behavioral effects, elevation showed a significant negative association with trunk heating rate (General Linear Model;

$\beta \pm SE = -0.12 \pm 0.04$, $p < 0.05$; Fig. 2e, Fig. S2, and Table S4). No significant relationship was observed for the head ($p = 0.10$), consistent with its primary role in sensory processing rather than thermal absorption. These results demonstrate that high-altitude *Phrynocephalus* species heat significantly faster than lowland species, a key thermoregulatory advantage that likely reduces basking duration and enhances opportunities for foraging, reproduction, and predator avoidance under cold-climate constraints. This pronounced divergence in thermal performance prompted further investigation into the underlying structural mechanisms driving enhanced heat gain at high elevation.

High-altitude lizards exhibit reduced spectral reflectance

Spectral reflectance provides a functional measure of how efficiently solar radiation is absorbed, offering insight into structural adaptations for thermoregulation across environmental gradients (*2*, *15*, *16*). Given that basking is a dominant thermoregulatory strategy in *Phrynocephalus* and that heating rate increases with altitude, we hypothesized that natural selection may favor reduced skin reflectance to increase solar energy absorption in colder habitats.

To test this hypothesis, reflectance spectra (196–1 100 nm) were recorded from seven populations spanning a broad elevational range, capturing both visible and NIR components of the solar spectrum. Notably, pronounced variation in both the magnitude and profile of reflectance were detected among populations (Fig. 2f). A marked elevational pattern emerged, with low-altitude *P. forsythii* (867 m) exhibiting the highest reflectance across both the head and trunk surfaces, while the two populations of highest-altitude species, *P. vlangalii* (4 189 m) and *P. erythrurus* (4 550 m), showed the lowest reflectance (Fig. 2f). This trend was most evident in the NIR range (700–1 100 nm), where low-elevation population reflected substantially more radiation than their high-altitude counterparts.

To quantify these patterns, pairwise Euclidean distances and cosine similarity were calculated to assess reflectance magnitude and spectral shape, respectively. For trunk NIR reflectance, Euclidean distances revealed strong clustering by altitude, with low-elevation *P. forsythii* diverging sharply and high-elevation populations forming a cohesive group (Fig. 2g). No such pattern was observed in the head region or in non-NIR wavelengths (Fig. S3a–c). Cosine similarity analysis further showed that NIR spectral shape was highly conserved across populations (most values > 0.8; Fig. S4a–b), whereas reflectance profiles in the non-NIR range were more variable (Fig. S4c–d), indicating that adaptation primarily affected reflectance magnitude rather than overall spectral form. These findings reveal that high-altitude *Phrynocephalus* populations exhibit significantly reduced NIR reflectance, a trait likely shaped by selection to improve solar energy capture. Depressed optical reflectivity in this spectral range offers a plausible mechanistic basis for elevated heating rates and may represent a critical adaptation for maintaining thermal performance in cold, high-elevation environments.

High-altitude lizards exhibit reduced skin light transmittance

Given that high-altitude lizards reflected less incoming solar radiation, skin transmittance was examined to determine whether solar energy passage through the integument was similarly constrained. *Ex vivo* light transmittance was measured across a broad spectral range (300–2 500 nm)

in skin samples from representative high- and low-altitude populations. Skin from high-altitude lizards displayed markedly lower transmittance across both visible and NIR wavelengths compared to low-altitude counterparts (Fig. S5). This pattern was consistent with the altitudinal clustering detected in Euclidean-distance analyses of transmission magnitude (Fig. S6a–b). In contrast, cosine similarity analysis indicated strong conservation of transmission spectral shape across populations (Fig. S6c–d), indicating that divergence occurred primarily through changes in transmission magnitude rather than alterations in intrinsic optical behavior. Taken together, reflectance and transmittance measurements showed that integument from high-altitude lizards functioned as a highly efficient energy-retaining layer, characterized by enhanced absorption and reduced light penetration. These dual optical properties would favor retention of solar energy within skin tissue, providing a mechanistic basis for the accelerated heating rates observed in high-elevation populations.

Elevation-associated increases in skin melanin contribute to reduced reflectance

To identify structural drivers of reduced reflectance, skin melanin content was quantified, given its broad-spectrum light absorption across ultraviolet (UV) and visible wavelengths (*28*). Histological analyses of trunk skin revealed a clear positive association between elevation and melanin content (Fig. 3a–c). Bayesian phylogenetic mixed-effects modeling confirmed a robust elevation effect ($\beta = 0.556$, 95% CI [0.241, 0.881]), indicating progressive darkening of skin with increasing altitude (Fig. 3c, Fig. S7, Table S5). Melanin content also exhibited a pronounced phylogenetic signal (Blomberg's $K = 1.018$, 95% CI [0.866, 1.199]; Fig. S8), consistent with evolutionary conservatism across species. Despite this constraint, individual-level variation accounted for the largest proportion of modeled variance ($\beta = 0.771$, 95% CI [0.604, 0.976]), surpassing species-level effects ($\beta = 0.219$, 95% CI [0.007, 0.803]; Fig. S7 and Table S5), indicating substantial within-population heterogeneity. After controlling for both phylogenetic structure and individual variation, melanin content consistently increased with elevation. This elevation-dependent melanization provides a mechanistic explanation for the reduced UV and visible reflectance observed at high altitude and supports enhanced solar energy absorption under cold environmental conditions.

Epidermal microstructural variation along elevational gradients

Although melanin strongly attenuated reflectance in the UV and visible spectra, its influence diminished in the NIR range, prompting investigation into the potential role of skin surface microstructures, which are known to modulate light in other systems (*17*, *29*, *30*). Scanning electron microscopy (SEM) of trunk scales from representative low- and high-altitude species revealed a surface nanostructure distributed across the epidermis (Fig. 3d), with feature dimensions on the scale of NIR wavelengths, consistent with optical interference or anti-reflective function.

To assess structural divergence, transmission electron microscopy (TEM) was used to quantify cross-sectional morphology (Fig. 3e–f). Comparative analysis revealed a clear elevational gradient in nanostructure morphology (Fig. 3g). High-altitude species exhibited significantly deeper nanostructures (L3) and a lower width-to-depth ratio (L1/L3) relative to lowland counterparts, which possessed broader, shallower configurations (Tukey's HSD; all $p < 0.05$; Fig. 3g and Table S6–7). These changes imply a directional morphological shift toward deeper and more elongated

nanostructures with increasing altitude—features consistent with enhanced solar energy trapping through reduced NIR reflectance.

Phylogenetic analysis confirmed strong phylogenetic conservatism in these traits (Blomberg's $K \approx 1$ and $p < 0.05$ for all traits like L1, L3 and L1/L3; Fig. S9), indicating that structural variation closely tracks lineage history. Given the well-established elevational expansion of this clade (*21*), the observed morphological gradient is unlikely to result from random divergence. Instead, the progressive refinement of epidermal nanostructures likely represents an adaptive innovation for maximizing solar energy retention, facilitating thermal performance and habitat colonization in cold, high-altitude environments on the Tibetan Plateau.

Nanostructural architecture functions as a broadband anti-reflective coating

To elucidate how epidermal nanostructures influence NIR reflectance, optical simulations were conducted based on morphological parameters derived from high- and low-altitude lizard populations. These structures were composed of weakly absorbing β-keratin and a periodic array of nanoscale pits (500 nm, Fig. 4a), embedded within a thin layer only a few hundred nanometers thick. Given that this periodicity fell below the infrared wavelength range (>700 nm), the nanostructure was modeled using effective medium theory to analyze its optical properties (Fig. 4b), which approximates the array as a homogeneous film characterized by an effective refractive index (n_{eff}) and height (h). The n_{eff}, estimated at 1.245 based on a measured duty cycle of 25%, was determined by the volume fraction of β-keratin and air. Height h, corresponding to the physical pit depth, was significantly greater in high-altitude lizards (250 nm) than in low-altitude populations (150 nm).

Reflectance modeling demonstrated that both skin types exhibited markedly reduced near-infrared reflectivity compared to a smooth keratin surface (4.6%), with values falling below 0.1% due to the periodic nanostructure (Fig. 4c). The enhanced antireflective performance of high-altitude skin was attributed to changed pit depth and shape, which enabled greater infrared penetration and thus more effective energy capture—consistent with empirical absorption patterns (*31*, *32*); Fig. S10). These structures act as infrared-selective antireflective coatings that suppress reflection within the NIR spectrum while remaining ineffective in the visible range (Fig. 4d). This wavelength selectivity arises from the breakdown of effective medium theory at visible wavelengths, where pit dimensions approximate the wavelength of incident light, leading to destructive scattering and loss of coherence. Consequently, visible reflectance remains high, suggesting that thermoregulation in this spectral band is achieved not via nanostructural manipulation but through melanin-based absorption mechanisms that preserve visual camouflage.

Notably, the antireflective function of the nanostructured epidermis also proved robust across a wide range of incident angles (Fig. 4e). Simulations showed that subwavelength pit arrays maintained low reflectivity at oblique angles exceeding 50°, ensuring stable optical performance despite variation in solar orientation due to changes in posture (e.g., crawling, basking, climbing) or time of day (*33*, *34*). This angular tolerance prevents functional collapse of antireflective capacity under natural behavioral and environmental conditions. Additionally, macroscopic roughness on the cm-to-mm scale may further suppress surface reflection by inducing multiple internal scattering events. This increase in optical path length enhances absorption within underlying water-rich tissue layers, significantly improving total absorption efficiency under broadband solar exposure.

Nanostructured skin enhances both thermal insulation and mechanical resilience

Efficient thermoregulation requires not only effective solar energy absorption but also sustained heat retention through the suppression of rapid dissipation. From a thermal perspective, the porous, network-like nanostructure may impede air convection within the epidermis, thereby limiting convective heat loss. Considering the stark contrast in thermal conductivity between *β*-keratin (~0.25 W/(m·K)) and air (~0.026 W/(m·K)) (*35*, *36*), even a nanostructured layer only several hundred nanometers thick can provide insulation comparable to a solid *β*-keratin layer several micrometers deep, effectively mitigating conductive heat loss to the external environment (Fig. S11). In addition to thermal benefits, this microarchitectural arrangement is expected to enhance mechanical integrity. The interconnected framework likely increases compressive modulus and structural robustness, conferring resistance to deformation and abrasion under environmental stress. This dual functionality offers adaptive advantages in high-altitude habitats where thermal extremes and mechanical challenges co-occur.

Discussion

Through integration of biological, optical, and physical methodologies, this study demonstrated that high-altitude lizards employ a composite thermoregulatory strategy to enhance solar energy absorption and suppress heat loss in alpine environments (Fig. 1). This adaptation involves a synergistic combination of melanin accumulation and specialized epidermal nanostructures.

Integumentary manipulation of NIR radiation via microstructures has emerged as a key innovation in thermal ecology. However, prior examples predominantly reflect adaptations for heat avoidance in arid climates. For instance, Saharan silver ants deploy triangular, corrugated hairs to enhance NIR reflectance for thermal avoidance (*15*), while certain avian and lepidopteran species utilize cuticular nanostructures to enhance NIR reflectance under high solar load (*2*, *16*, *37*, *38*). In contrast, the epidermal nanostructures identified in this study consisted of densely arrayed pits bordered by micro-ridges (Fig. 3d), forming a distinct morphological system to minimize NIR reflectance. These findings suggest fundamentally distinct light-matter interaction regimes underpinning radiative control, with structural absorption favored over reflectance. Although effective medium theory provided a useful framework to interpret NIR suppression, further discoveries may prompt refinement of novel photonic models and inform design of next-generation biomimetic optical materials.

Our findings revealed that melanin and nanostructures together constitute a dual-spectrum absorption system, enabling effective capture of solar radiation across both visible and NIR bands. At the Earth's surface, visible and NIR wavelengths each contribute approximately 50% of incident solar energy (*8*). While dark pigmentation enhances absorption of visible light in many cold-adapted ectotherms (*12*, *39*), the addition of skin nanostructures allows lizards to exploit the remaining NIR component while simultaneously minimizing conductive heat loss. This integration permits fine-tuned radiative control, conferring thermoregulatory advantages critical to sustaining activity and energy efficiency in high-elevation habitats. The coordinated deployment of pigment-based and structure-based spectral control mechanisms exemplifies a high-efficiency solution to thermal

challenges in extreme environments.

These findings support a broader reassessment of melanin function in high-altitude adaptation. Beyond its established role in enhancing solar absorption under cold conditions, elevated melanin likely reflects additional selective pressures, including UV protection at high elevations (*28*, *40*, *41*) and compensation for increased visible reflectance caused by nanostructures. Modeling demonstrated that pit arrays strongly suppressed NIR reflectance but concurrently increased reflectance in the visible spectrum (Fig. 4d), a shift that could elevate predation risk by making individuals more visually conspicuous. Thus, elevated melanin levels may have evolved not only to enhance heat absorption and provide UV protection, but also to counteract this increased visibility by absorbing more visible light. This proposed "camouflage-compensation" hypothesis suggests that melanin plays a critical role in balancing the thermoregulatory benefits of nanostructures with their potential ecological costs, underscoring the need for further investigation into the ecological drivers of melanin variation.

In conclusion, comparative analysis of viviparous *Phrynocephalus* lizards demonstrated that high-altitude species have evolved a highly integrated skin-based thermal management system that offsets severe alpine thermal constraints. This system enables accelerated heating through the synergistic effects of increased melanin, which enhances visible light absorption and a previously unrecognized nanostructured array that functions as an efficient anti-reflective coating for NIR light. Simultaneously, this nanostructure provides effective insulation that reduces conductive heat loss. Together, these adaptations reveal a novel integumentary mechanism that selectively modulates NIR energy flux, exposing an overlooked axis of thermal adaptation with broad ecological and evolutionary implications (*8*). The multifunctionality, spectral selectivity, and angle-independence of this biological design offer compelling principles for advanced material engineering, particularly for lightweight, energy-efficient thermal regulation technologies.

Acknowledgement

We thank Prof. Shilong Yang (Northeast Forestry University) for providing infrared camera, and Zeng Jiang and Ligui Tang for their assistance with fieldwork sampling. We are grateful to Prof. Huai Chen, Prof. Yuchi Zheng and Prof. Weizhao Yang (Chengdu Institute of Biology), as well as Prof. Yang Li and Dr. Jian Chen (Nanjing Hangkong University) for their valuable research suggestions.

Fundings

This research was supported by the Second Tibetan Plateau Scientific Expedition and Research Program (STEP, Grant No. 2019QZKK0402) and the National Natural Science Foundation of China (Grant Nos. 62450123 and 62375042).

References:

1. B. J. Sinclair, K. E. Marshall, M. A. Sewell, D. L. Levesque, C. S. Willett, S. Slotsbo, Y. Dong, C. D. G. Harley, D. J. Marshall, B. S. Helmuth, R. B. Huey, Can we predict ectotherm responses to climate change using thermal performance curves and body temperatures?

Ecology Letters **19**, 1372–1385 (2016).

2. I. Medina, E. Newton, M. R. Kearney, R. A. Mulder, W. P. Porter, D. Stuart-Fox, Reflection of near-infrared light confers thermal protection in birds. *Nat Commun* **9**, 3610 (2018).

3. L. M. Carrascal, P. López, J. Martín, A. Salvador, Basking and Antipredator Behaviour in a High Altitude Lizard: Implications of Heat-exchange Rate. *Ethology* **92**, 143–154 (1992).

4. J. A. Díaz, Ecological correlates of the thermal quality of an ectotherm's habitat: a comparison between two temperate lizard populations. *Functional Ecology* **11**, 79–89 (1997).

5. J. Clavel, H. Morlon, Accelerated body size evolution during cold climatic periods in the Cenozoic. *Proceedings of the National Academy of Sciences* **114**, 4183–4188 (2017).

6. Z. Xu, W. You, Y. Zhou, W. Chen, Y. Wang, T. Shan, Cold-induced lipid dynamics and transcriptional programs in white adipose tissue. *BMC Biol* **17**, 74 (2019).

7. F. N. Hamada, M. Rosenzweig, K. Kang, S. R. Pulver, A. Ghezzi, T. J. Jegla, P. A. Garrity, An internal thermal sensor controlling temperature preference in Drosophila. *Nature* **454**, 217–220 (2008).

8. D. Stuart-Fox, E. Newton, S. Clusella-Trullas, Thermal consequences of colour and near-infrared reflectance. *Philosophical Transactions of the Royal Society B: Biological Sciences* **372**, 20160345 (2017).

9. M. Royer, C. Meyer, J. Royer, K. Maloney, E. Cardona, C. Blandino, G. Fernandes da Silva, K. Whittingham, K. N. Holland, "Breath holding" as a thermoregulation strategy in the deep-diving scalloped hammerhead shark. *Science* **380**, 651–655 (2023).

10. T. S. Fristoe, J. R. Burger, M. A. Balk, I. Khaliq, C. Hof, J. H. Brown, Metabolic heat production and thermal conductance are mass-independent adaptations to thermal environment in birds and mammals. *Proceedings of the National Academy of Sciences* **112**, 15934–15939 (2015).

11. B. G. Lovegrove, A phenology of the evolution of endothermy in birds and mammals. *Biological Reviews* **92**, 1213–1240 (2017).

12. B.-J. Sun, W.-M. Li, P. Lv, G.-N. Wen, D.-Y. Wu, S.-A. Tao, M.-L. Liao, C.-Q. Yu, Z.-W. Jiang, Y. Wang, H.-X. Xie, X.-F. Wang, Z.-Q. Chen, F. Liu, W.-G. Du, Genetically Encoded Lizard Color Divergence for Camouflage and Thermoregulation. *Molecular Biology and Evolution* **41**, msae009 (2024).

13. D.-G. Luo, W. W. S. Yue, P. Ala-Laurila, K.-W. Yau, Activation of Visual Pigments by Light and Heat. *Science* **332**, 1307–1312 (2011).

14. A. M. Franklin, K. J. Rankin, A. Hugall, D. Stuart-Fox, Exposure to thermal extremes favors higher solar reflectivity in intertidal gastropods. *iScience* **25**, 105674 (2022).

15. N. N. Shi, C.-C. Tsai, F. Camino, G. D. Bernard, N. Yu, R. Wehner, Keeping cool: Enhanced optical reflection and radiative heat dissipation in Saharan silver ants. *Science*, doi: 10.1126/science.aab3564 (2015).

16. C. Kang, S. Im, W. Y. Lee, Y. Choi, D. Stuart-Fox, B. Huertas, Climate predicts both visible and near-infrared reflectance in butterflies. *Ecology Letters* **24**, 1869–1879 (2021).

17. J. Teyssier, S. V. Saenko, D. van der Marel, M. C. Milinkovitch, Photonic crystals cause active colour change in chameleons. *Nat Commun* **6**, 6368 (2015).

18. L.-Y. Wang, A. Franklin, J. Black, D. Stuart-Fox, Heating rates are more strongly influenced by near-infrared than visible reflectance in beetles. *Journal of Experimental Biology* **224** (2021).

19. E. N. Solovyeva, V. S. Lebedev, E. A. Dunayev, R. A. Nazarov, A. A. Bannikova, J. Che, R. W. Murphy, N. A. Poyarkov, Cenozoic aridization in Central Eurasia shaped diversification of toad-headed agamas (Phrynocephalus; Agamidae, Reptilia). *PeerJ* **6**, e4543 (2018).

20. L. Cui, R. A. Nazarov, Y. Chen, Y. Qi, X. Guo, Y. Xia, W. Yang, Whole genome sequencing reveals the phylogenetic relationship and reticulate evolution of Phrynocephalus lizards in Eurasia. bioRxiv [Preprint] (2025). https://doi.org/10.1101/2025.09.09.675123.

21. X. Guo, Z. Yao, B. Cai, X. Xiao, Q. Xu, Y. Chen, L. Cui, X. Qiu, J. Fu, Y. Qi, W. Yang, Genomic insights into the reticulate evolution of viviparous *Phrynocephalus* lizards on the Qinghai-Tibetan Plateau. *Molecular Phylogenetics and Evolution* **211**, 108404 (2025).

22. D. Bauwens, P. E. Hertz, A. M. Castilla, Thermoregulation in a Lacertid Lizard: The Relative Contributions of Distinct Behavioral Mechanisms. *Ecology* **77**, 1818–1830 (1996).

23. J. A. Díaz, R. Izquierdo-Santiago, A. Llanos-Garrido, Lizard thermoregulation revisited after two decades of global warming. *Functional Ecology* **36**, 3022–3035 (2022).

24. A. Bertoia, J. Monks, C. Knox, A. Cree, A nocturnally foraging gecko of the high-latitude alpine zone: Extreme tolerance of cold nights, with cryptic basking by day. *Journal of Thermal Biology* **99**, 102957 (2021).

25. M. Kechnebbou, J. Belliure, M. Chammem, Field Thermoregulatory Behavior in the African Spiny-Tailed Lizard Uromastyx acanthinura. *Ichthyology & Herpetology* **113** (2025).

26. G. Deconninck, N. Meyer, H. Colinet, S. Pincebourde, Thermal Preference Plasticity in Ectotherms: Integrating Temperature Affinity and Thermoregulation Precision. *The American Naturalist* **206**, 247–260 (2025).

27. R. Megía-Palma, O. Jiménez-Robles, J. A. Hernández-Agüero, I. De la Riva, Plasticity of haemoglobin concentration and thermoregulation in a mountain lizard. *Journal of Thermal Biology* **92**, 102656 (2020).

28. G. Zonios, A. Dimou, I. Bassukas, D. Galaris, A. Tsolakidis, E. Kaxiras, Melanin absorption spectroscopy: new method for noninvasive skin investigation and melanoma detection. *JBO* **13**, 014017 (2008).

29. J. G. Murillo, J. Rodríguez-Romero, J. A. Medina-Vázquez, E. Y. González-Ramírez, C. Álvarez-Herrera, H. Gadsden, Iridescence and thermal properties of Urosaurus ornatus lizard skin described by a model of coupled photonic structures. *J. Phys. Commun.* **4**, 015006 (2020).

30. S. V. Saenko, J. Teyssier, D. Van Der Marel, M. C. Milinkovitch, Precise colocalization of interacting structural and pigmentary elements generates extensive color pattern variation in Phelsumalizards. *BMC Biology* **11**, 105 (2013).

31. J.-Q. Xi, M. F. Schubert, J. K. Kim, E. F. Schubert, M. Chen, S.-Y. Lin, W. Liu, J. A. Smart, Optical thin-film materials with low refractive index for broadband elimination of Fresnel reflection. *Nature Photon* **1**, 176–179 (2007).

32. L. Zhou, Y. Tan, J. Wang, W. Xu, Y. Yuan, W. Cai, S. Zhu, J. Zhu, 3D self-assembly of aluminium nanoparticles for plasmon-enhanced solar desalination. *Nature Photon* **10**, 393–398 (2016).

33. Y.-F. Huang, S. Chattopadhyay, Y.-J. Jen, C.-Y. Peng, T.-A. Liu, Y.-K. Hsu, C.-L. Pan, H.-C. Lo, C.-H. Hsu, Y.-H. Chang, C.-S. Lee, K.-H. Chen, L.-C. Chen, Improved broadband and quasi-omnidirectional anti-reflection properties with biomimetic silicon nanostructures. *Nature Nanotech* **2**, 770–774 (2007).

34. Q. Yang, X. A. Zhang, A. Bagal, W. Guo, C.-H. Chang, Antireflection effects at nanostructured material interfaces and the suppression of thin-film interference. *Nanotechnology* **24**, 235202 (2013).

35. Y. Xue, S. Lofland, X. Hu, Thermal Conductivity of Protein-Based Materials: A Review. *Polymers* **11**, 456 (2019).

36. Y.-S. Ma, F.-M. Kuo, T.-H. Liu, Y.-T. Lin, J. Yu, Y. Wei, Exploring keratin composition variability for sustainable thermal insulator design. *International Journal of Biological Macromolecules* **275**, 133690 (2024).

37. D. Stuart-Fox, E. Newton, R. A. Mulder, L. D'Alba, M. D. Shawkey, B. Igic, The microstructure of white feathers predicts their visible and near-infrared reflectance properties. *PLOS ONE* **13**, e0199129 (2018).

38. A. Krishna, X. Nie, A. D. Warren, J. E. Llorente-Bousquets, A. D. Briscoe, J. Lee, Infrared optical and thermal properties of microstructures in butterfly wings. *Proc. Natl. Acad. Sci. U.S.A.* **117**, 1566–1572 (2020).

39. S. Clusella-Trullas, J. H. Wyk, J. R. Spotila, Thermal benefits of melanism in cordylid lizards: a theoretical and field test. *Ecology* **90**, 2297–2312 (2009).

40. M. Brenner, V. J. Hearing, The Protective Role of Melanin Against UV Damage in Human Skin. *Photochemistry and Photobiolgy* **84**, 539–549 (2008).

41. D. F. Zamudio Díaz, L. Busch, M. Kröger, A. L. Klein, S. B. Lohan, K. R. Mewes, L. Vierkotten, C. Witzel, S. Rohn, M. C. Meinke, Significance of melanin distribution in the epidermis for the protective effect against UV light. *Sci Rep* **14**, 3488 (2024).

Figure captions

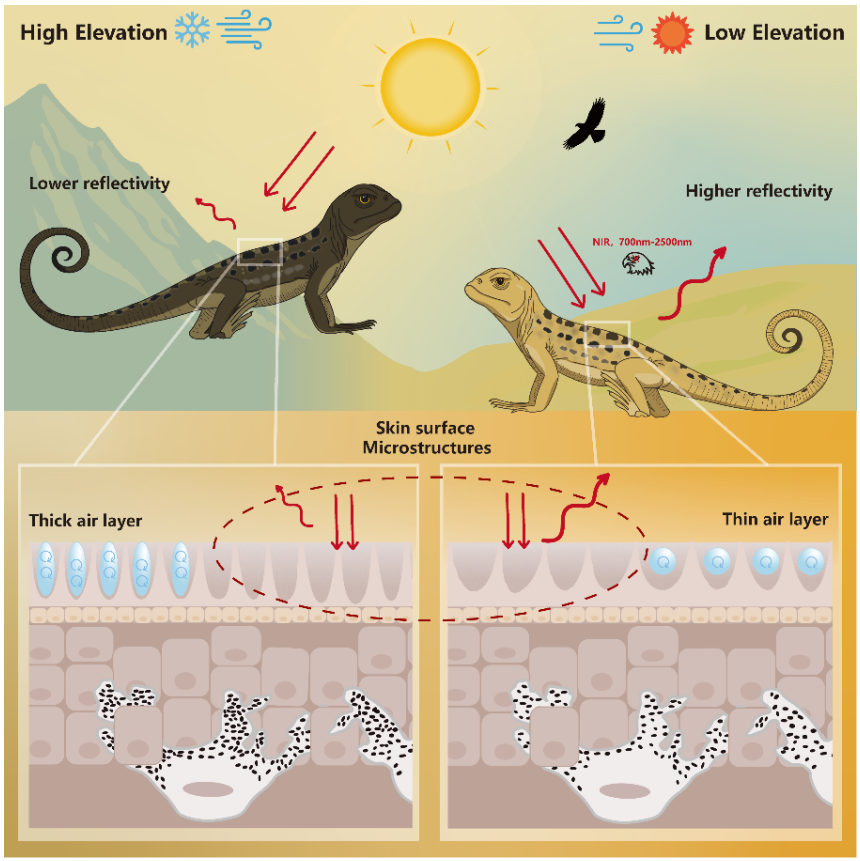

Fig. 1. Skin-based structural and optical adaptations in high-altitude lizards enable enhanced visible light and near-infrared (NIR) absorption, accelerated heating, and reduced thermal dissipation. The microstructure on the skin surface forms a NIR antireflective layer. Melanin beneath the epidermis absorbs visible light. At the same time, the epidermal microstructure effectively traps air to create a thermal insulation layer.

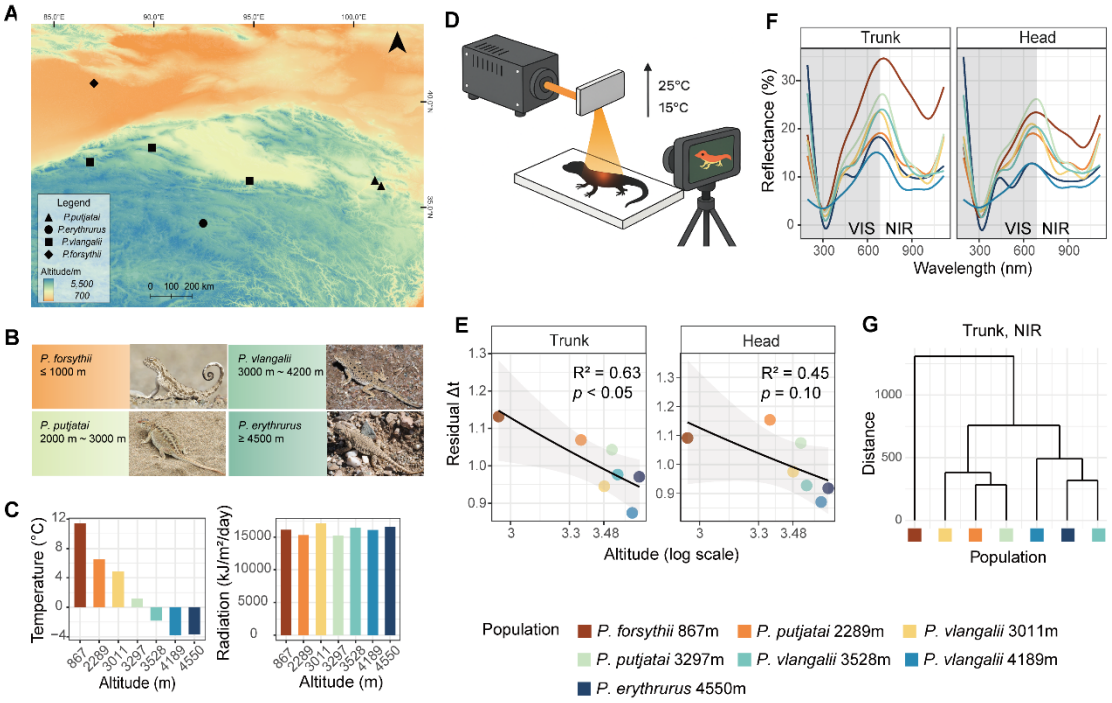

Fig. 2. Elevation-associated variation in thermoregulatory performance and skin optical properties among *Phrynocephalus* species. (A–B) Sampling covered seven populations across four species spanning elevations from 867 m to 4 550 m. **(C)** Mean annual temperature of population locations decreased with elevation, whereas solar radiation remained relatively stable. **(D)** Schematic depicting experimental assay used to evaluate heating efficiency as body temperature increased from 15°C to 25°C, employing a full-spectrum artificial light source and an infrared camera to illuminate and record thermal responses. **(E)** High-altitude lizard populations attained target body temperature more rapidly than lowland counterparts. Each point represented the mean of a population. The semi-transparent shaded area indicated the model's confidence interval. R-squared indicated the explanatory power of the linear model, and the *p* value showed the statistical significance of the elevation factor. **(F)** Head and trunk reflectance in the visible (VIS, < 700 nm) and near-infrared (NIR, $\geqslant 700$ nm) range exhibited lower values in high-elevation populations. **(G)** Hierarchical clustering of populations based on Euclidean distances of spectral reflectance demonstrated population-level similarity in near-infrared (NIR) reflectance of the trunk.

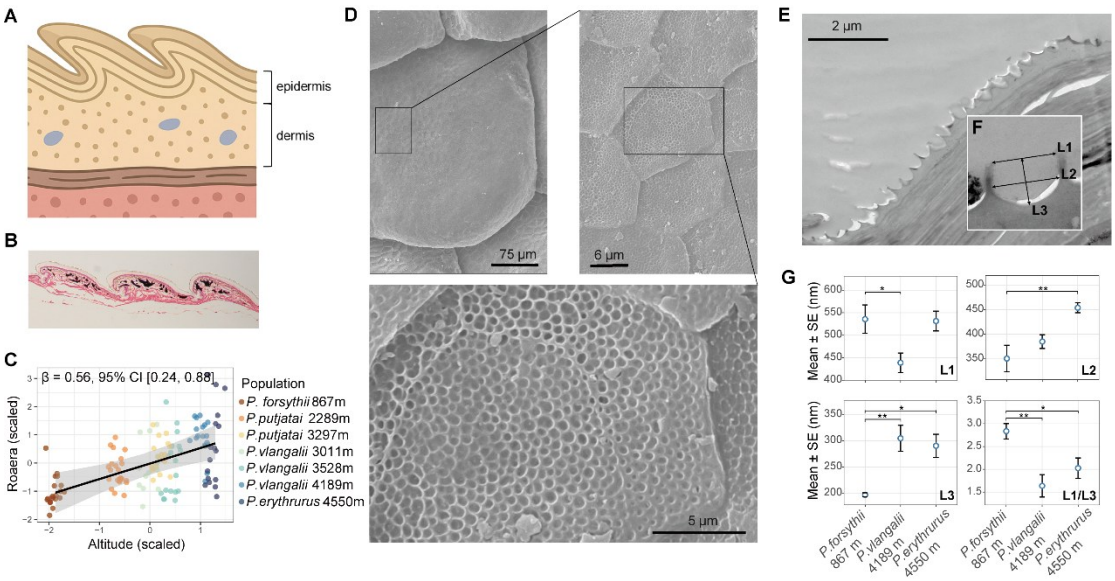

Fig. 3. Microstructural and pigmentary differences in trunk skin of lizards across elevational gradients. (A) Schematic of skin architecture showing melanin distribution in the dermis and microstructures in the outer epidermis. **(B)** H&E-stained paraffin section highlighting melanin pigmentation in trunk skin. **(C)** Melanin content (Roaera) increased with elevation. The β value represented the effect of elevation on melanin content in the model, accompanied by a 95% confidence interval. **(D)** SEM images showing distinct nanostructures on the skin surface. **(E)** TEM images showing cross-sectional morphology of nanostructures. **(F)** Morphological parameters include aperture (L1), ventral diameter (L2), and depth (L3). The L1/L3 ratio was used as a morphological descriptor. **(G)** Morphological traits of nanostructures among populations, with high-altitude lizards exhibiting deeper pits (larger L3) and smaller L1/L3 ratios (*$p < 0.05$, **$p < 0.01$).

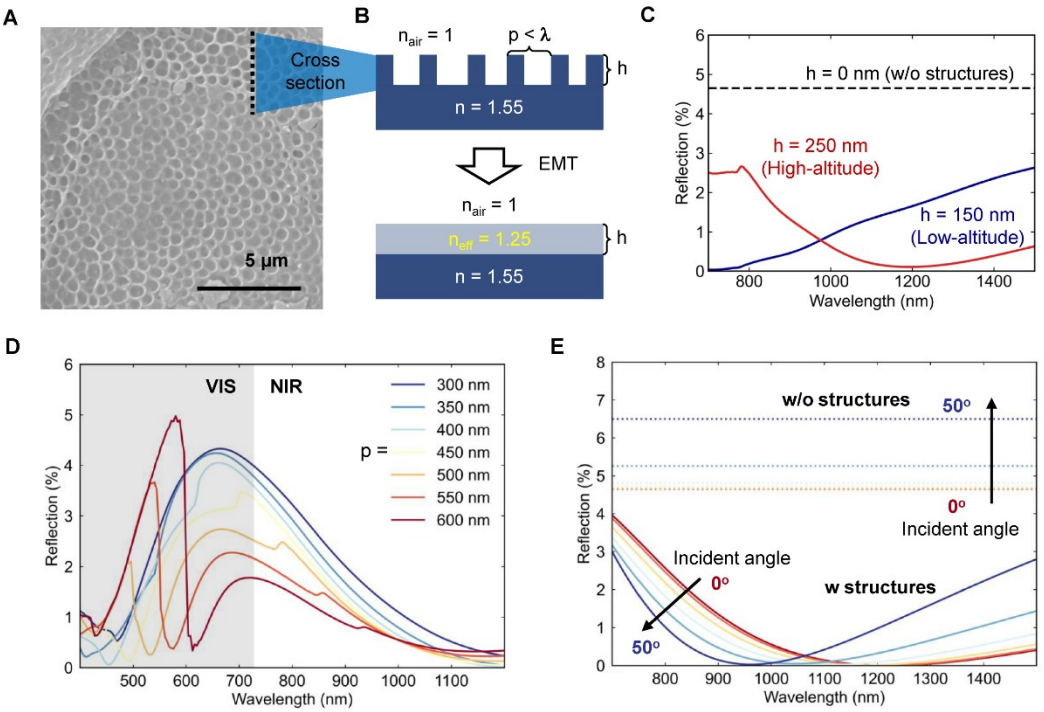

463

464 **Fig. 4. Optical modeling of epidermal nanostructures and their anti-reflective performance.**
465 **(A)** SEM images showing quasi-periodic array of nanoscale pit structures (inset: schematic cross-
466 section). **(B)** Effective medium theory (EMT) model approximating the structured surface as a
467 homogeneous thin film with effective refractive index n_{eff}. **(C)** Simulated reflectivity spectra
468 comparing surfaces with no structures, lowland structures, and highland structures, confirming
469 enhanced antireflective performance in highland morphologies. **(D)** Simulated reflectivity spectra
470 for nanostructures with varying pit dimensions across visible (VIS) and near-infrared (NIR) bands,
471 demonstrating wavelength-selective antireflective behavior. **(E)** Simulated reflectivity spectra for
472 structured and unstructured surfaces across a range of incident angles, indicating robust
473 antireflective performance under oblique incidence.

Supplementary

Materials and methods

Animals capturing and husbandry

A total of 43 toad-head agama lizards (*Phrynocephalus*) were captured by noose from July to August in 2023. The lizards came from 7 populations with altitudes ranged from 867 m to 4550 m above sea level (Fig. 2a-b and table S1).

Table S1. Details of each sampled population.

Population	Specie	Altitude/m	Longitude/°	Latitude/°	Samples
P. forsythia 867 m	*P. forsythii*	867	86.99728	40.87853	6 (♂4, ♀2)
P. vlangalii 3528 m	*P. vlangalii*	3528	89.90023	37.81753	6 (♂6)
P. vlangalii 3011 m	*P. vlangalii*	3011	94.78564	36.2467	6 (♂6)
P. vlangalii 4189 m	*P. vlangalii*	4189	86.80045	37.13979	6 (♂3, ♀3)
P. erythrurus 4550 m	*P. erythrurus*	4550	92.46499	34.23679	6 (♂5, ♀1)
P. putjatai 3297 m	*P. putjatai*	3297	101.0621	36.28012	6 (♂4, ♀2)
P. putjatai 2289 m	*P. putjatai*	2289	101.3723	36.01296	6 (♂3, ♀4)

All animals were transported to the Chengdu Institute of Biology (Chengdu, Sichuan province) and housed under standardized conditions for approximately two weeks before subsequent experiments. Each population was housed in plastic box with dimensions of 50 cm (length) × 35 cm (width) × 45 cm (height) and with a 10 cm layer of fine sand at the bottom. Each population was fed every other day with an ample supply of mealworms as food, which were mixed with powder of calcium and a compound vitamin before feeding. Each box was equipped with a basking lamp (40w), with a light-dark cycle of 12 h. Every 2 to 3 days, water was sprayed onto the sand as drinking water and to maintain moisture in the lower substrate. The temperature of the environment was kept in 25 ± 1 ℃, with a relative air humidity level of 55 % ~ 65 %.

All sampling was approved separately by the Forestry and Grassland Bureaus of Xizang Autonomous Region, Xinjiang Uygur Autonomous Region, and Qinghai province (approved No. included 2023-115 and 2023-13). All experiments with animals followed the approved protocols of the Animal Care and Use Committee, Chengdu Institute of Biology, Chinese Academy of Sciences (approved No. is 20230405).

Environmental temperature and solar radiation

Temperature and solar radiation reflect the thermal conditions experienced by local lizards. To evaluate thermal environments along the altitudinal gradient, we extracted annual temperature, wind speed (monthly and annual) and solar radiation (monthly and annual) based on the sampling coordinates. We downloaded bioclimatic variables (GeoTIFF format), monthly wind speed, and monthly solar radiation data at a 30-arc-second resolution (~1 km²) from the WorldClim database

(*1*), which provides climate data for the period 1970–2000. We then extracted annual mean temperature (BIO1) from the bioclimatic variables at the sampling site coordinates to represent the thermal conditions of each population. We also extracted the radiation values based on sampling coordinates too, and calculated the annual mean radiation value to represent solar radiation condition for lizards. Data of wind speed was processed with the same protocol as solar radiation data. All data extraction from GeoTIFF files was performed using the R package (*2*).

Testing for heating up rate

To compare body heating rates among lizard populations, we conducted thermal experiments and recorded the time required (Δt) for body temperature to increase. Before the experiments commenced, each lizard was individually placed in an insulated box containing ice packs, with care taken to prevent direct contact with the ice packs to avoid frostbite. We monitored individual body temperatures using an infrared thermometer, starting the experiment when lizard body temperatures dropped below 15 ℃. Each Lizard was secured with thin noose around the neck and rear waist, with the other end of the noose fixed on either side of an insulating expanded polystyrene board. This arrangement kept the lizard body flat on the board, minimizing movement during the experiment. We utilized an artificial light-sources with full wavelength band (Power source: 7IPX500P; Light source: SOFN, 7ILX150P; 200-2500 nm wavelengths, controlled in 250W during experiments), directed onto the board via mirrors, concurrently illuminating the whole lizard dorsal surface. Simultaneously, an infrared thermal camera (Testo SE & Co. KGaA, Testo 890) was used to record lizard body temperature, with fixed measurement points at the top of the head and at two locations on the top of trunk surface (central trunk and lower trunk) for real-time temperature monitoring. Recordings began when the lizard body temperature reached its highest point 15 ℃ and stopped when the lowest temperature reached 25 ℃. We recorded the duration time Δt (s) that different body parts reached 25 ℃. Each lizard underwent two rounds of experiments in each of two continued days and the order of experimental individuals was randomized on both days. The room temperature during the experiments was at 25 ± 1 ℃, with air humidity maintained between 50% to 60%. Once the thermal experiment concluded, we immediately measured the snout-vent length (SVL) of each individual using a caliper, with precision to 0.01mm.

Considering the characteristic plasticity of thermal traits, we firstly employed test of Intraclass Correlation Coefficients (ICCs) to ensure the repeatability of Δt within same individual and body part. Two-way random-effects model with absolute agreement and single-measurement type was employed. ICC values, 95% confidence intervals, F-statistics, and associated p-values were estimated with R package *irr* version 4.2.3 (*3*).

For temperature metric, Δt of trunk is the mean value between central trunk and lower trunk. Before comparison of Δt values, we tested phylogenetic signal of Δt by calculating Blomberg's K value. To incorporate phylogenetic information into subsequent analyses, a species-level phylogenetic tree was first pruned to match the species present in the dataset. The original tree was read and trimmed to exclude taxa not represented in the data (*4*). The resulting pruned tree was visualized to confirm its structure. A phylogenetic variance–covariance matrix was then constructed from the pruned tree and converted into a sparse matrix format for downstream analysis. To assess the phylogenetic signal in Δt values, species-level mean values and standard errors were calculated for head and trunk. Blomberg's K was then computed for each trait using the pruned phylogenetic

tree. Significance testing was performed to evaluate whether trait similarity among species was greater than expected under a Brownian motion model of evolution. The phylogenetic test was conducted with R package *phytools* version 2.4.4 (*5*).

A two-step analysis was conducted to evaluate the relationship between Δt values and environmental elevation at population level while accounting for individual variation. First, for each temperature trait (Δt of head and trunk), General Linear Models (GLMs) were fitted at the individual level with log-transformed Δt as the response and log-transformed SVL and sex as predictors. The residuals from these models, representing body size- and sex-corrected trait values on a log scale, were extracted for each individual. Next, residuals were averaged within each population, and population-level mean residuals were regressed against log-transformed mean elevation in General linear models (GLMs). This approach allowed assessment of whether variation in Δt across populations was associated with elevation, independent of body size and sex effects. Model assumptions, including normality of variance and homoscedasticity, were checked and found to be met without significant violations.

Spectral reflectance of skin

The reflectance spectrum indicates how animals utilize solar radiation. Subsequently, we employed a spectrometer (Ocean optics, MAYA2000pro) to measure the reflective spectrum of lizard skin. Measurements were taken on the dorsal surfaces of the head and trunk. On the head, three points were randomly selected, while six points were randomly selected on the central trunk and lower trunk. Mean values of each body part were used in analysis. To ensure the standardization of reflectance measurement, we used a ring sleeve with length of 1.5 cm at the end of the optical probe and ensure it vertically contacted animal skin in a fixed distance of 5 mm (*6*). Reflectance spectra were calculated as percentage (%).

To quantify the magnitude differences and shape difference of reflectance spectra among populations, we computed Euclidean distance matrices and cosine similarity at wavelength of UV/visible (< 700 nm) and NIR range (700 nm - 1100 nm), by grouping in head and trunk. Euclidean distance quantifies the straight-line separation between two spectral vectors in a high-dimensional space and inherently reflects differences in their reflective intensities. It was computed using the base R function *dist()* with the Euclidean method, applied to the transposed matrix so that distances were calculated between populations rather than between wavelengths. Cosine similarity, by contrast, measured the cosine of the angle between two spectral vectors, reflecting the similarity in spectral shape while being insensitive to absolute reflectance magnitude. It was calculated using R package *lsa* version 0.73.3 (*7*).

Animal euthanizing and skin tissues sampling

After measurements of skin reflective spectrum, lizards were euthanized through intraperitoneal injection with an over dose of 5% pentobarbital sodium solution (*8*). Animals were judged as death when they close eyes and did not have any reaction. The muscles of left leg were preserved in 75% ethanol solution for phylogenomic analysis in another project (Published as (*4*)). The skin on dorsal trunk was peeled off without other tissues, fixed in 2.5% glutaraldehyde (phosphate buffer, pH 7.0–7.5; Servicebio, G1124-100ML), and stored at 4 °C until further

processing.

Testing for transmission variation of skin

The fixed skin of three representative populations (*P. forsythia* 867 m, *P. vlangalii* 4189 m, and *P. erythrurus* 4550 m) was employed to evaluate the transmission variation along elevational gradient. A spectrophotometer (PerkinElmer, Lambda 950, UV/Vis/NIR) was used to measure the individual transmission spectrum. The wavelength range for measurement was set from 300nm to 2500nm. Prior to measurement, the instrument was warmed up and auto-zeroed with the transmission port open, as recommended for direct transmission mode. Fixed skin samples were dried with absorbent paper and mounted directly in the transmission beam path using the sample holder. A blank reference measurement (e.g., air) was recorded before each series. Spectral scans were performed at ~2.0 nm resolution wavelength region, balancing resolution and signal-to-noise ratio. Transmission was calculated as percentage (%).

Paraffin method and melanin content

To explore the variation of skin melanin content along altitudinal gradient, we measured the relative quantity of melanin in skin using histological methods. As the trunk was the largest area for lizard to receive light radiation during sun basking, we used trunk skin for melanin quantification. Routine paraffin method was used to obtain sections of trunk skin

Skin samples with similar size were placed in a tissue processor and passed through an ethanol series to remove water gradually: 75% ethanol for 4 h; 85% ethanol for 2 h; 90% ethanol for 2 h; 95%; ethanol for 1 h. This was followed by two 30 min washes in absolute ethanol, then 5–10 min each in alcohol-benzene and xylene to fully clear the tissue. Finally, samples were infiltrated in molten paraffin wax at 65 °C in three successive baths, each for 1 hour, to ensure complete wax penetration. Next, the wax-soaked tissue pieces were transferred into embedding frames pre-filled with melted paraffin. While still pliable, each sample was oriented properly, labeled, and placed into a mold. The block was cooled on a –20 °C freezing platform so that the wax hardened rapidly. Once solid, the paraffin block was removed from the mold and any excess trimmed away. The trimmed paraffin block was mounted on a microtome and sliced into 4 μm thick sections. Each section was floated on a water bath set to 40 °C to facilitate gradual flattening. Carefully, slides were used to lift the sections from the water. The mounted slices were then baked at 60 °C to fully adhere and dry. After the wax surface fully hardened, the sections were stored at room temperature, ready for histological staining and analysis.

Paraffin sections were first immersed in two successive environmentally-friendly dewaxing solution baths, each for 20 min. Then they were passed through an ethanol series in this order: 100% ethanol (anhydrous I) for 5 min; 100% ethanol (anhydrous II) for 5 min; 75% ethanol for 5 min. After this, the slides were thoroughly rinsed under running tap water to rehydrate the tissues. All sections were treated with HD Constant Staining Pretreatment Solution for exactly 1min. This step helps improve staining uniformity and clarity. Slides were immersed in hematoxylin solution for 3–5 min to stain nuclei. They were then dipped briefly into hematoxylin differentiation solution to remove excess dye, followed by a rinse with running tap water. Next, slides were placed in hematoxylin bluing solution to adjust the color tone, and rinsed again with tap water. Sections were

briefly passed through 95% ethanol for 1 min. Immediately after, they were stained in eosin dye for 15 s before being swiftly transferred to the next step. Slides were dehydrated through a graded series of solvents, each for 2 min: 100% ethanol I; 100% ethanol II; 100% ethanol III; Normal butanol I; Normal butanol II; Xylene I; Xylene II. Finally, sections were cover slipped using neutral mounting medium to preserve the tissue and staining.

For each individual, 3 to 4 non-consecutive sections were randomly obtained for subsequent measurements. We examined and took photos of each section with a microscope (Nikon Ei). As the field of vision for the microscope is smaller than the skin section, we took multiple photos of each section, and make sure each pair of adjacent photos had enough overlapping region for following joint treatment. Thus, each skin section had 3 to 12 photos. Then, we merged photos within each section that overlap into a seamless panorama using ImageJ (version 1.54p), via the plugin *MosaicJ* (*9–11*). After that, the images were visually inspected for sharpness and any ghosting to verify correct alignment. Tiles that failed in automatic stitching were manually adjusted: the overlapping regions of two images were visually overlaid and their relative positions were fine-tuned until maximum clarity and no ghosting were achieved. The images were then merged and exported. The next, to calculate the relative quantity of skin melanin, we measured proportion of melanin area ration to skin area. With ImageJ, we selected the skin tissue section and removed any unwanted background introduced by stitching the images. We then converted the image to 16-bit grayscale. To measure the total section area, we operated the threshold tool and adjusted the sliders until the entire tissue section was highlighted, then calculated the resulting area. Next, we adjusted the same threshold sliders so that only the melanin deposits were selected, and recorded this melanin area. Finally, we calculated the relative melanin content by dividing the melanin area by the total section area (ROaera). All quantifications were carried out exclusively by Yao ZY.

To examine the association between ROaera and elevation while accounting for phylogenetic relatedness, a Bayesian phylogenetic mixed-effects model was fitted using the R package *brms* version 2.22.0 (*12*). The response variable (ROaera) and elevation were standardized (Z-score transformation) prior to analysis. The model included elevation as a fixed effect, species as a phylogenetic random effect informed by a correlation matrix derived from the pruned phylogenetic tree, and individual identity as a non-phylogenetic random effect to account for repeated measures. The model was run with four Markov chains for 5000 iterations each, using weakly informative priors. Posterior estimates of fixed and random effects, including phylogenetic signal (variance among species), were extracted and summarized to assess the influence of elevation and the contribution of phylogenetic structure to trait variation. Model convergence was verified by inspecting trace plots.

During the experimental protocol, two sections from two individuals failed and were excluded from the skin melanin analysis; consequently, three backup sections from three individuals were included. We evaluated phylogenetic signal by calculating Blomberg's K value with bootstrap method and R package *phytools* as before. To assess the robustness of phylogenetic signal in ROaera, a non-parametric bootstrap approach was employed. For each of 5000 iterations, one individual was randomly sampled with replacement from each species to generate a trait vector representing interspecific variation. Blomberg's K was then calculated for each bootstrap replicate using the pruned phylogenetic tree. Replicates that failed due to missing or incompatible data were excluded. The mean and 95% percentile confidence interval of the resulting K distribution were used to estimate the strength and uncertainty of the phylogenetic signal in the trait.

Observation on skin microstructures via SEM and TEM

The remaining trunk skin of each lizard was divided into two portions for microstructural observation using scanning electron microscopy (SEM) and transmission electron microscopy (TEM). Samples preparation methods for SEM and TEM followed standardized protocol.

Tissues for SEM were washed three times with 0.1 M phosphate buffer (PB, pH 7.4) for 15 min each, followed by post-fixation in 1% osmium tetroxide (OsO_4) prepared in 0.1 M PB (pH 7.4) at room temperature for 1–2 h. The tissues were then rinsed three times in 0.1 M PB for 15 min each. Tissues then were dehydrated through a graded ethanol series at room temperature: 30%, 50%, 70%, 80%, 90%, and 95% ethanol for 15 min each, followed by two changes of 100% ethanol (15 min each). Tissues were next transferred to isoamyl acetate for 15 min. Dehydrated tissues were subjected to critical point drying using a critical point dryer (Quorum K850). Dried tissues were mounted onto metallic stubs using carbon adhesive stickers and sputter-coated with a thin layer of gold for 30 s (Lon sputtering apparatus, Hitachi MC1000) to ensure surface conductivity for SEM imaging. A SEM (Hitachi, SU8100) was used to observe and take photos for each individual skin tissue. Each prepared tissue had 6 to 7 photos with scales ranged from 1mm to 5μm.

To further reflect altitudinal variation, three representative populations (*P. forsythia* 867 m, *P. vlangalii* 4189 m, and *P. erythrurus* 4550 m) were chosen for further observation with TEM. Tissue samples for TEM were post-fixed in 1% osmium tetroxide (OsO_4) prepared in 0.1 M phosphate buffer (PB, pH 7.4) for 2 h at room temperature in the dark. Following post-fixation, the OsO_4 solution was removed, and tissues were rinsed three times with 0.1 M PB (pH 7.4), each rinse lasting 15 min. Dehydration was performed at room temperature using a graded ethanol series: 30%, 50%, 70%, 80%, and 95% ethanol for 20 min each, followed by two changes of 100% ethanol for 20 min each. The samples were then transferred through two changes of acetone for 15 min each. For resin infiltration, tissues were incubated in a 1:1 mixture of acetone and EMBed 812 resin at 37 °C for 2–4 h, followed by a 1:2 acetone: EMBed 812 mixture overnight at 37 °C. This was followed by immersion in pure EMBed 812 for 5–8 h at 37 °C. The tissues were then embedded in fresh EMBed 812 resin within embedding molds and kept at 37 °C overnight. Polymerization was carried out by transferring the embedding molds to a 60 °C oven for over 48 h. Once polymerized, the hardened resin blocks were removed from the molds and stored at room temperature until further processing. For positioning, the resin blocks were trimmed and sectioned into 1.5 μm semi-thin slices using a microtome (ultra microtome, Leica UC7; diamond slicer, Daitome Ultra 45°). These sections were stained with toluidine blue and examined under a light microscope to identify the region of interest. Ultrathin sections (60–80 nm thick) were cut using an ultramicrotome and collected onto 150-mesh copper grids coated with formvar film. For contrast enhancement, sections were stained with 2% uranyl acetate in saturated alcohol solution for 8 min in the dark, followed by three rinses in 70% ethanol and three in ultrapure water. This was followed by staining with 2.6% lead citrate for 8 min in a CO_2-free environment, and again rinsed three times in ultrapure water. The stained grids were gently blotted dry with filter paper and allowed to dry completely overnight at room temperature. A TEM (Hitachi HT7800) was employed to take photos of skin surface. Five fields of view were acquired for each observation target, with scale ranges of 5 μm to 500 nm for surface.

To compare the variation of skin micro structures among high and low populations, we measured the morphology of these pits including caliber (L1), waist caliber (L2), and depth (L3). The caliber was measured as the diameter across the top of the pit opening, measured between its

two endpoints. Waist caliber was the diameter measured at the midpoint of the pit. And depth was the vertical distance from the opening plane down to the pit deepest point. The ration from L1 to L3 was also calculated to reflect the shape of pits. More than 13 pits of each lizard individual were measured (One lizard was only measured with 9 pits because the relative worse quality of TEM).

To test whether measured traits varied among populations, linear mixed-effects models (LMM) were fitted for each trait (L1, L2, L3, and L1/L3) using R package *lme4* version 1-1.35.3 (*13*). In each model, population was included as a fixed effect and individual ID was included as a random intercept to account for repeated measurements within individuals. As the population and species was one-to-one correspondence, species was not added into the models to avoid multicollinearity. Prior to analysis, all trait values and elevation were Z-standardized. Fixed-effect estimates and associated statistics were extracted to evaluate population-level differences in each trait. To further explore pairwise differences among populations, we conducted post hoc Tukey's HSD comparisons with R package *emmeans* version 1.11.0 (*14*), obtaining pairwise contrasts from each model with population as the grouping factor.

To evaluate the phylogenetic signal in measured traits of microstructures, a non-parametric bootstrap procedure was implemented. For each of 5000 iterations, one measurement per species was randomly sampled with replacement to construct a species-level trait vector. Blomberg's K was calculated for each replicate using the species phylogeny. Bootstrap replicates with computational errors were excluded. The mean and 95% percentile confidence interval of the resulting K distribution were used to assess the strength and uncertainty of the phylogenetic signal. All statistical analyses in this study were conducted in R version 4.2.2 (*15*).

Physical modeling and simulation

Optical simulations were performed using the commercial software FDTD Solutions to investigate the optical properties of the sand lizard's surface microstructures. To simplify the modeling of the irregular morphology, the surface was approximated as a two-dimensional (2D) periodic array of square holes, with the unit cell was illustrated in Fig.S1. Given the negligible intrinsic absorption of the constituent β-keratin in the visible and near-infrared spectral regions, the extinction coefficient was ignored, and the material was modeled with a constant real refractive index of 1.55. In the simulation domain, periodic boundary conditions (PBC) were applied in the in-plane (x and y) directions to simulate the infinite array, while perfectly matched layers (PML) were imposed along the propagation direction (z) to eliminate boundary reflections. The structure was excited by a normally incident broadband plane wave polarized along the x-axis (transverse magnetic, TM polarization). Notably, due to the C4 rotational symmetry of the unit cell, the optical response calculated under TM polarization was equivalent to that under unpolarized sunlight, to which the sand lizard was actually exposed.

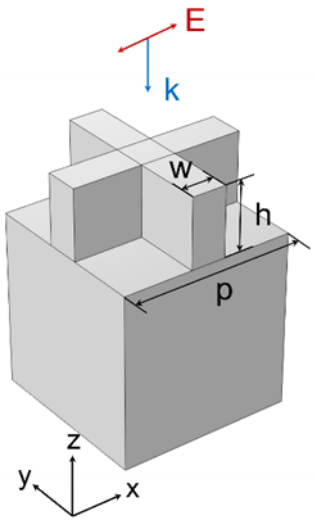

Figure S1. Schematic of the unit cell for the simplified microstructure model. The surface morphology was modeled as a periodic array of square holes, where w, p and h denoted the ridge width (w = 100 nm), structural period (p = 500 nm) and pit height, respectively. The material was set as β-keratin with a refractive index of 1.55.

Supplementary results

Heating rate

According to the results of tests for Intraclass Correlation Coefficients (ICCs), the Δt showed good repeatability across body parts, with the Δt of central trunk exhibiting the highest consistency (Table S2). ICCs were 0.759 for the head (95% CI [0.590, 0.864]), 0.867 for the central trunk (95% CI [0.754, 0.928]), and 0.770 for the lower trunk (95% CI [0.613, 0.869]). F-tests indicated each ICC was significantly greater than zero (head, F (42,36.34) = 7.85, $p < 0.05$; central trunk, F (42,30.74) = 15.6, $p < 0.05$; lower trunk, F (42,42.18) = 7.57, $p < 0.05$).

Table S2. Results of tests for Intraclass Correlation Coefficients showed good repeatability of heating rate across body parts.

Parameter	ICC	95% CI	F test	*p* value
Δt of head	0.759	[0.590, 0.864]	F (42,36.3400321240011) = 7.85	<0.05
Δt of central trunk	0.867	[0.754, 0.928]	F (42,30.7388487229624) = 15.6	<0.05
Δt of lower trunk	0.770	[0.613, 0.869]	F (42,42.1783743982363) = 7.57	<0.05

Blomberg's K and associated significance tests indicated no detectable phylogenetic signal in Δt values, suggesting no phylogenetic constraint on heating rate (Table S3). Specifically, Δt measured at the head showed K = 0.951 (p = 0.483), and Δt measured at the trunk region showed K = 0.955 (p = 0.508).

Table S3. Test results of phylogenetic signal for Δt values indicated no phylogenetic constraints on heating rate.

Trait	K value	*p* value

Δt of head	0.951203	0.483
Δt of trunk	0.955488	0.508

The results of General Linear Models indicated the effect of altitude on the heating rate of the trunk body surface (Table S4 and Fig. S2). For the trunk region, altitude had a significant negative effect on heating rate ($\beta = -0.121 \pm 0.042$, $p < 0.05$), and the model explained a substantial proportion of variance ($R^2 = 0.63$). In contrast, for the head region, the effect of altitude was negative but not statistically significant ($\beta = -0.125 \pm 0.062$, $p = 0.10$), with a moderate model fit ($R^2 = 0.45$).These results indicated that lizards from higher altitudes exhibited faster trunk heating.

Table S4. Results of General Linear Models indicated significant effect of altitude on heating rate of trunk part.

Trait	Predictor	β	SE	Statistic	p value	R^2	R^2_{adj}
Head	Intercept	0.985882	0.494030	1.995593	0.102515	0.446120	0.335344
Head	Altitude	-0.124680	0.062128	-2.006790	0.101059	0.446120	0.335344
Trunk	Intercept	0.958357	0.330453	2.900132	0.033786	0.628944	0.554733
Trunk	Altitude	-0.120980	0.041557	-2.911200	0.033353	0.628944	0.554733

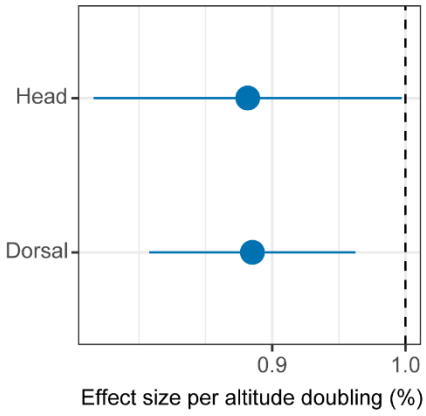

Figure S2. Effect size of altitude on residual Δt values sensitivity for the head and trunk regions. Effect sizes represented the proportional change in temperature sensitivity per altitude doubling (mean ± 95% CI). Value of trunk showed a slight decrease in sensitivity with increased altitude (effect size < 1), and confidence intervals had no overlap with unity, indicating significant effects.

Skin reflectance

Euclidean distances were computed using Euclidean metrics of mean reflectance spectra, and clusters were generated by hierarchical agglomerative clustering. Populations from similar altitudes tended to group together in near-infrared wavelength for trunk (Fig. 2g), indicating convergent reflectance properties along the elevational gradient. The separation between high- and low-altitude populations was more pronounced in the NIR range for trunk (Fig. 2g) than for head (Fig. S3a), and also than in the UV–VIS range (Fig. S3b–c), suggesting stronger altitude-associated divergence in infrared optical traits.

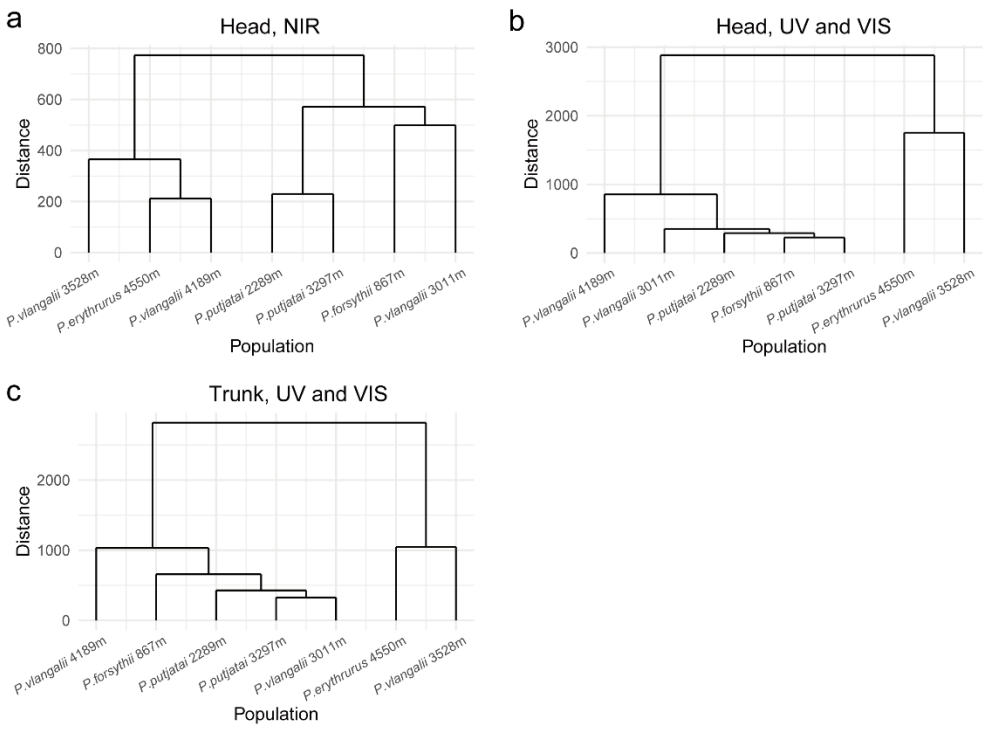

Figure S3. Hierarchical clustering of populations based on Euclidean distances of spectral reflectance across wavelengths and body regions. (a) Dendrograms showed population similarity in NIR reflectance for head. (b-c) Corresponding clustering patterns were based on UV – VIS reflectance for head and trunk.

Pairwise cosine similarity compared the spectral reflectance of the seven sampled lizard populations. For NIR wavelength range across body parts, cosine similarity was generally high, ranging from 0.85 to 1.0 (Fig. S4a-b). In contrast, for UV-VIS wavelength range across body parts, cosine similarity was lower and more variable (scale 0.4 to 1.0; Fig. S4c-d).

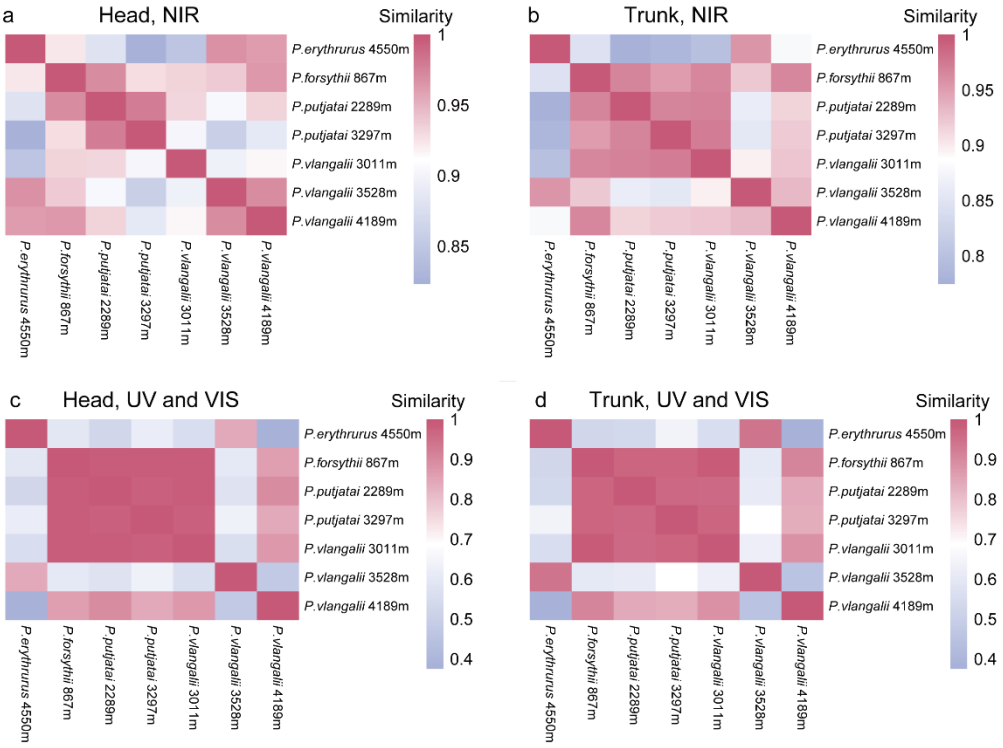

Figure S4. Cosine similarity heatmaps of spectral reflectance from different populations across wavelength range and body parts. (a-b) Similarity was based on NIR reflectance data from head and trunk, respectively. (c-d) Similarity was based on combined UV-VIS reflectance data from the head and trunk, respectively. The color scale indicated similarity, with dark red represented the highest similarity (1.0) and blue represented the lowest (0.4 or 0.85, depending on the panel).

Skin transmission

Trunk skin of high-altitude lizards showed markedly lower transmittance across both visible and NIR wavelengths compared to lowland relatives (Fig. S5). Meanwhile, divergence in spectral properties of transmission was assessed via both Euclidean distance and pairwise cosine similarity. Hierarchical clustering consistently separated *P. forsythii* from the *P. erythrurus* and *P. vlangalii* cluster across both wavelength ranges (Fig. S6a-b). Crucially, the magnitude of divergence was significantly greater in the NIR range, where Euclidean distances reached approximately 100 units, compared to a maximum of 15 units in the UV-VIS range. Pairwise cosine similarity was universally high (ranging from 0.992 to 1.0), reflecting the conserved spectral shape divergence (Fig. S6c-d).

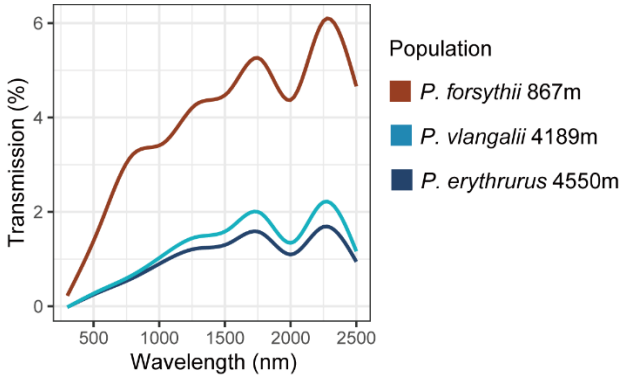

Figure S5. Transmission spectra indicated reduced skin transmittance across 300–2 500 nm wave

range in highland lizards. Each line represented mean value of measured transmission.

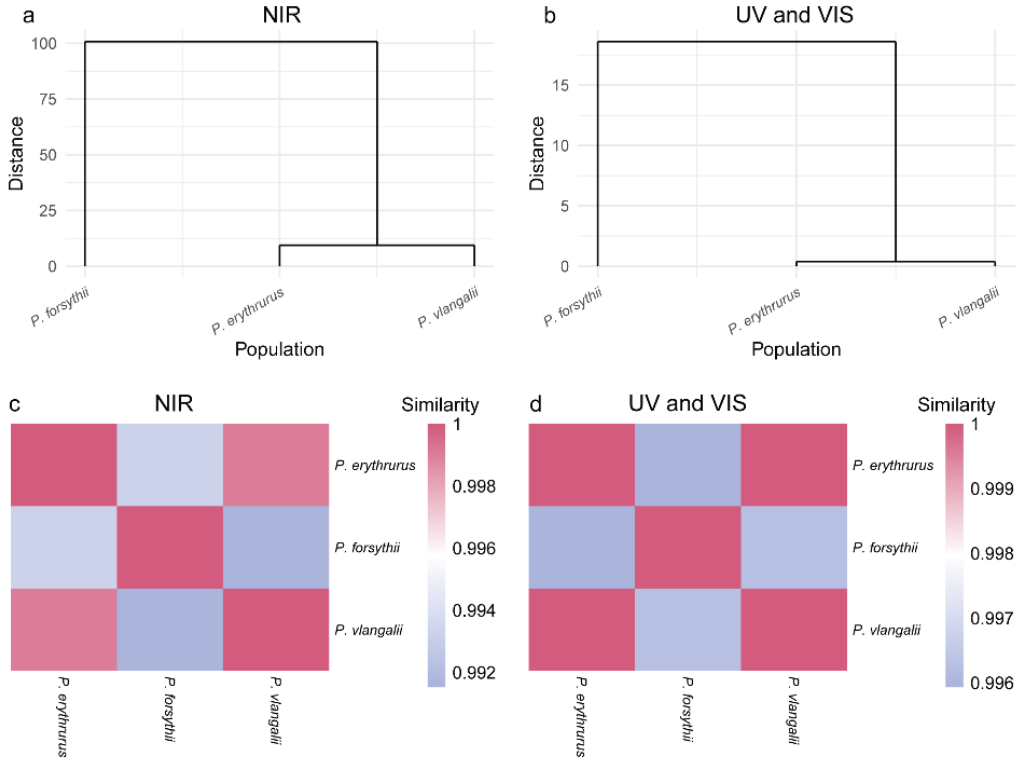

Figure S6. Divergence in transmission spectrum between high and low lizard populations based on NIR and UV-VIS wavelengths. (a-b) The results of hierarchical agglomerative clustering were based on Euclidean distance of mean spectra for three populations. Panel (a) shows clustering using NIR, and panel (b) shows clustering using UV-VIS. (c-d) The pairwise cosine similarity matrix compared the mean reflectance spectra for the three populations in the NIR and UV-VIS ranges, respectively. Similarity was generally extremely high, with a narrow scale (0.992 to 1.0 for NIR; 0.996 to 1.0 for UV-VIS).

Skin melanin content

Results from the Bayesian phylogenetic mixed-effects model indicated a significant positive effect of altitude on skin melanin content (ROaera, β = 0.556, 95% CI [0.241, 0.881]; Table S5 and Fig. S7). Since the 95% CI for the altitude effect did not overlap zero, it was credible that increased altitude was associated with greater skin melanin content. Furthermore, the largest variation in the model was attributed to differences among individuals (β = 0.771, 95% CI [0.604, 0.976]), followed by the residual variation (β = 0.414, 95% CI [0.357, 0.484]). The variation explained by the species effect was the smallest (β = 0.219, 95% CI [0.007, 0.803]).

Table S5. Results of Bayesian phylogenetic mixed-effects model indicated the effect of altitude on skin melanin content.

Response	Parameter	*β*	Est.Error	95% CI
ROaera	Intercept	-0.014	0.208615	[-0.414, 0.409]
ROaera	Altitude	0.556	0.161610	[0.241, 0.881]
ROaera	SD (individual)	0.771	0.096097	[0.604, 0.976]
ROaera	SD (species)	0.219	0.213288	[0.007, 0.803]

ROaera	SD (residual)	0.414	0.032632	[0.357, 0.484]

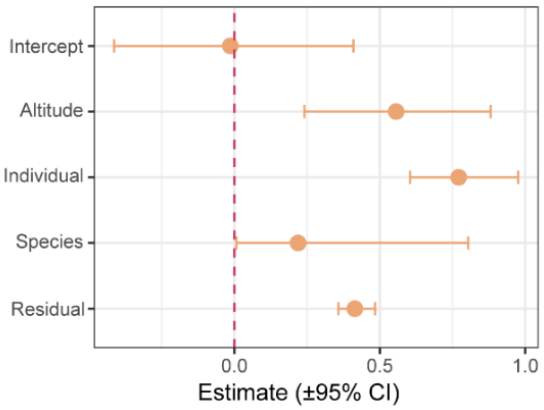

Figure S7. Parameter estimates and 95% credible intervals for the Bayesian phylogenetic mixed-effects model. The plot displayed the estimated parameter values and their corresponding 95% CI for the fixed effect (intercept, altitude) and the standard deviations (SD) of the random effects (individual, species, and residual). The dashed vertical line indicated a parameter estimate of zero.

The phylogenetic signal for skin melanin content (ROaera) was assessed using Blomberg's K statistic. The observed mean K value was 1.018, and the corresponding 95% bootstrap confidence Interval was determined to be 0.866 to 1.199 (Fig. S8). Since the 95% CI encompasses 1.0, the phylogenetic signal for ROaera was not significantly different from the expectation under a Brownian Motion model of evolution, suggesting that the trait evolved gradually in proportion to phylogenetic history.

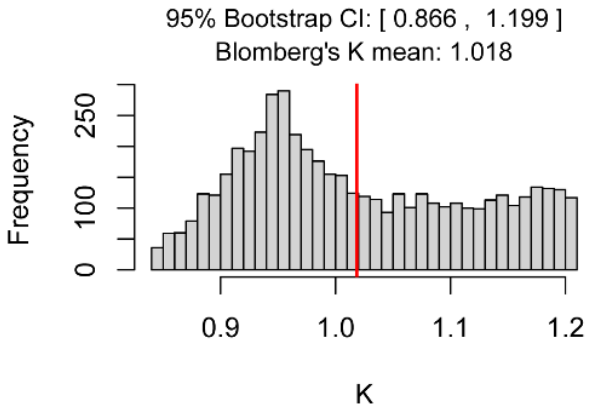

Figure S8. Bootstrap distribution of Blomberg's K statistic for skin melanin content. The histogram illustrated the distribution of Blomberg's K values generated through a bootstrap resampling procedure. The red vertical line marked the observed mean K value. The top annotation displayed the 95% bootstrap confidence interval.

Skin microstructures

Linear mixed-effects models and post hoc Tukey's HSD tests revealed significant inter-population variation in skin microstructure morphology (Table S6-7). Specifically, the low-altitude *P. forsythii* population (867m) exhibited significantly lower mean values for L3 compared to the high-altitude lizard population. Furthermore, the L1/L3 ratio showed the strongest divergence, being significantly higher in *P. forsythii* (867m) than in both high-altitude populations.

Table S6. Results of linear mixed-effects models (LMM) indicated the variation of skin microstructure morphology (L1, L2, L3, and L1/L3) among lizard Populations.

Response	Parameter	*β*	SE	Statistic	*p* value
L1	Population (*P.forsythii* 867m)	0.041071	0.250252	0.164117	0.871704
L1	**Population (*P.vlangalii* 4189m)**	**-0.61175**	**0.248019**	**-2.46653**	**0.025857**
L2	**Population (*P.forsythii* 867m)**	**-0.83335**	**0.222677**	**-3.7424**	**0.001847**
L2	**Population (*P.vlangalii* 4189m)**	**-0.55025**	**0.220074**	**-2.50029**	**0.024617**
L3	**Population (*P.forsythii* 867m)**	**-0.92021**	**0.276052**	**-3.33348**	**0.004222**
L3	Population (*P.vlangalii* 4189m)	0.13032	0.274497	0.474759	0.641535
L1/L3	**Population (*P.forsythii* 867m)**	**0.820091**	**0.311674**	**2.631244**	**0.018435**
L1/L3	Population (*P.vlangalii* 4189m)	-0.3854	0.310525	-1.24112	0.233177

Table S7. Post hoc Tukey's honest significant difference (HSD) comparisons of skin microstructure morphology between lizard populations.

Response	Parameter	*β*	SE.	df	t value	*p* value
L1	*P.erythrurus* 4550m vs *P.forsythii* 867m	-0.04107	0.250396	15.27443	-0.16402	0.985292
L1	*P.erythrurus* 4550m vs *P.vlangalii* 4189m	0.611747	0.248175	14.72775	2.464985	0.064606
L1	***P.forsythii* 867m vs *P.vlangalii* 4189m**	**0.652818**	**0.247891**	**14.80479**	**2.63349**	**0.047038**
L2	***P.erythrurus* 4550m vs *P.forsythii* 867m**	**0.833349**	**0.222885**	**15.31198**	**3.738919**	**0.005119**
L2	*P.erythrurus* 4550m vs *P.vlangalii* 4189m	0.550248	0.220301	14.5934	2.497713	0.061073
L2	*P.forsythii* 867m vs *P.vlangalii* 4189m	-0.2831	0.220105	14.77495	-1.28621	0.424341
L3	***P.erythrurus* 4550m vs *P.forsythii* 867m**	**0.920214**	**0.276121**	**15.20267**	**3.332652**	**0.011725**
L3	*P.erythrurus* 4550m vs *P.vlangalii* 4189m	-0.13032	0.274571	14.85963	-0.47463	0.884167
L3	***P.forsythii* 867m vs *P.vlangalii* 4189m**	**-1.05053**	**0.274272**	**14.85718**	**-3.83027**	**0.004457**
L1/L3	***P.erythrurus* 4550m vs *P.forsythii* 867m**	**-0.82009**	**0.311709**	**15.14497**	**-2.63095**	**0.046685**
L1/L3	*P.erythrurus* 4550m vs *P.vlangalii* 4189m	0.385398	0.310562	14.92137	1.240968	0.448592

L1/L3	***P.forsythii* 867m**	**vs**	**1.205489**	**0.310295**	**14.89811**	**3.884977**	**0.003978**
	***P.vlangalii* 4189m**							

The phylogenetic signals for all four skin microstructure parameters (L1, L2, L3, and L1/L3 ratio) were assessed using the Blomberg's K statistic. The mean K values for all traits were consistently close to 1.0 (Fig. S9). Furthermore, the 95% bootstrap confidence intervals for all four parameters encompassed the value of 1.0 (Fig. S9). This finding indicated that the evolution of all measured skin microstructure traits was not significantly different from the expected pattern under a Brownian Motion model, suggesting that these traits evolved gradually in proportion to phylogenetic history.

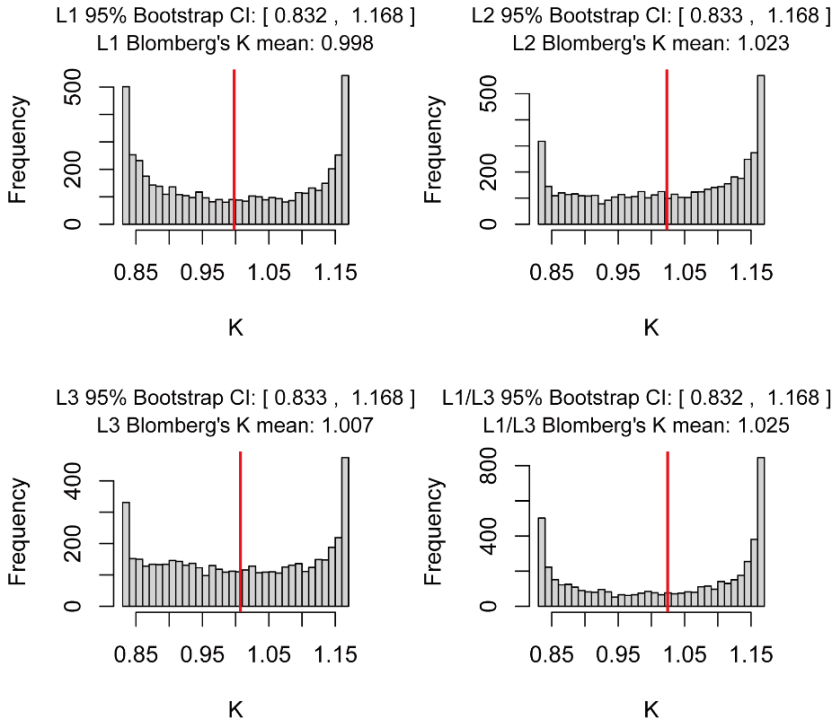

Figure S9. Bootstrap distribution of Blomberg's K statistic for four skin microstructure morphology parameters (L1, L2, L3, and L1/L3 ratio). The red vertical line in each panel marked the observed mean K value, and the corresponding 95% bootstrap confidence interval (95% CI) was indicated in the title of each panel. K values of 1.0 indicated a pattern of evolution consistent with the Brownian Motion model.

Effect of pit height on infrared anti-reflection performance

As described in the main text, given that the periodicity of these microstructures was approximately several hundred nanometers, smaller than the NIR wavelength, Effective Medium Theory (EMT) indicated that they functioned as an anti-reflective coating. By tailoring their geometry (e.g., fill factor and height), the microstructures minimized surface reflection to maximize NIR light transmission into the skin. Specifically, the effective refractive index (n_{eff}) of the microstructure was determined by its fill factor. The optimal anti-reflection effect was achieved

when the pit height (h) of the microstructure, a key morphological parameter for distinguishing populations at different elevations, satisfied $n_{eff} \cdot h = \lambda/4$. Our further investigation into the height-dependent NIR reflectance revealed that sand lizards inhabiting higher altitudes, characterized by larger pit height, exhibited lower total reflectance across the entire NIR band (Fig. S10). The actual absorption was effectively facilitated by the strong intrinsic absorption of water molecules in the underlying tissue. This induced a synergistic "transmission – penetration – absorption" sequence, which accounted for the exceptional anti-reflective properties observed.

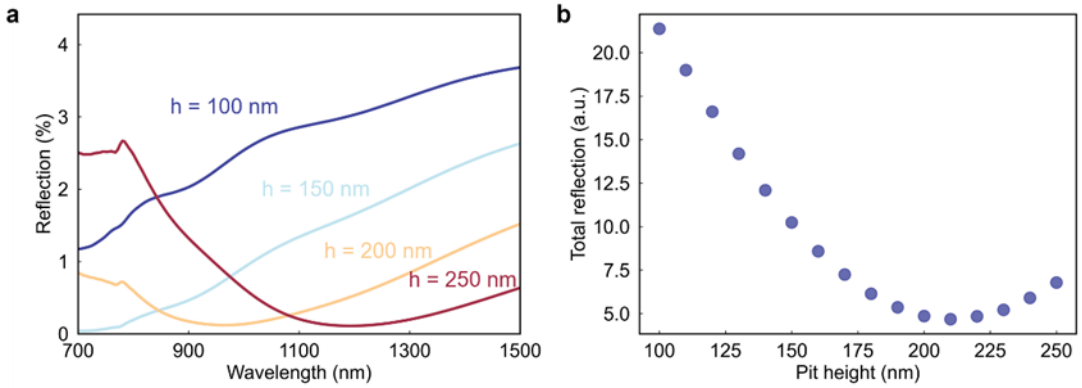

Figure S10. Simulations of the pit height-dependent NIR anti-reflection effect of the microstructure. (a) NIR reflectance spectra for various pit heights (h), illustrated height-dependent antireflective performance. (b) The total NIR reflectance across the entire NIR band, showed that an optimal antireflective effect was achieved at h = 210nm for a fill factor of 25%.

Microstructures serving as thermal insulation layers

As mentioned in the main text, given the nearly one-order-of-magnitude difference in thermal conductivity between β-keratin (~0.25 W/(m·K)) and air (~0.026 W/(m·K)), the microstructures of the skin surface may function as thermal insulation layers. On one hand, filling the interstitial spaces of the microstructures with a medium of lower thermal conductivity (such as air) reduced the effective thermal conductivity of the structural layer, thereby minimized heat loss due to thermal conduction. On the other hand, microstructures suppressed the velocity of airflow over the surface, reduced heat dissipation caused by thermal convection. To validate this hypothesis, we conducted thermal simulations via the commercial multi-physics software COMSOL to model the lizard's skin microstructures and to investigate the influence of pit height on thermal insulation performance under both windy (thermal convection-dominated) and wind-free (thermal conduction-dominated) conditions. In this model, the microstructure was heated with a constant power density of Q = 6.25 × 10^5 W/m² and was placed in an air environment with an ambient temperature of 5°C (Fig. S11a). The thermal insulation capability of the microstructure layer was evaluated based on the steady-state body temperature. As shown in Fig. S11b, the body temperature exhibited a monotonic increase with pit height under both environmental conditions, indicating an enhanced thermal insulation capability provided by the microstructure.

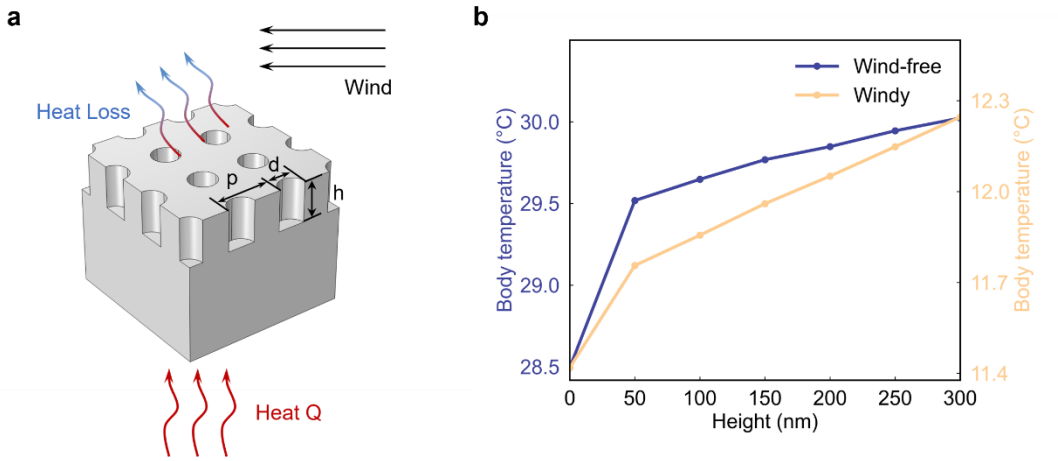

Figure S11. Simulation of the thermal insulation performance of surface microstructures. (a) Schematic of the simulation model, where *d, p* and *h* denoted the pit diameter (*d* = 300 nm), structural period (*p* = 400 nm) and the pit height, respectively. (b) Simulated body temperature of the lizard as a function of pit height, demonstrating the thermal insulation capability provided by the microstructures.

References

1. S. E. Fick, R. J. Hijmans, WorldClim 2: new 1-km spatial resolution climate surfaces for global land areas. *Int. J. Climatol* **37**, 4302–4315 (2017).

2. R. J. Hijmans, J. van Etten, M. Sumner, J. Cheng, D. Baston, A. Bevan, R. Bivand, L. Busetto, M. Canty, B. Fasoli, D. Forrest, A. Ghosh, D. Golicher, J. Gray, J. A. Greenberg, P. Hiemstra, K. Hingee, A. Ilich, I. for M. A. Geosciences, C. Karney, M. Mattiuzzi, S. Mosher, B. Naimi, J. Nowosad, E. Pebesma, O. P. Lamigueiro, E. B. Racine, B. Rowlingson, A. Shortridge, B. Venables, R. Wueest, raster: Geographic Data Analysis and Modeling, version 3.6-20 (2023); https://cran.r-project.org/web/packages/raster/index.html.

3. Matthias Gamer <m.gamer@uke.uni-hamburg.de>, Jim Lemon <jim@bitwrit.com.au>, Ian Fellows <ifellows@uscd.edu> Puspendra Singh <puspendra.pusp22@gmail.com>, irr: Various Coefficients of Interrater Reliability and Agreement, (2005); https://doi.org/10.32614/CRAN.package.irr.

4. X. Guo, Z. Yao, B. Cai, X. Xiao, Q. Xu, Y. Chen, L. Cui, X. Qiu, J. Fu, Y. Qi, W. Yang, Genomic insights into the reticulate evolution of viviparous *Phrynocephalus* lizards on the Qinghai-Tibetan Plateau. *Molecular Phylogenetics and Evolution* **211**, 108404 (2025).

5. L. J. Revell, phytools 2.0: an updated R ecosystem for phylogenetic comparative methods (and other things). *PeerJ* **12**, e16505 (2024).

6. B. Lu, Genetic Basis and Evolutionary Forces of Sexually Dimorphic Color Variation in a Toad-Headed Agamid Lizard. *Molecular Biology and Evolution* **41**, msae054 (2024).

7. lsa: Latent Semantic Analysis. https://CRAN.R-project.org/package=lsa.

8. Y. Wu, J. Fu, B. Yue, Y. Qi, An atypical reproductive cycle in a common viviparous Asia Agamid *Phrynocephalus vlangalii*. *Ecology and Evolution* **5**, 5138–5147 (2015).

9. J. Schindelin, I. Arganda-Carreras, E. Frise, V. Kaynig, M. Longair, T. Pietzsch, S. Preibisch, C. Rueden, S. Saalfeld, B. Schmid, J.-Y. Tinevez, D. J. White, V. Hartenstein, K. Eliceiri, P. Tomancak, A. Cardona, Fiji: an open-source platform for biological-image analysis. *Nat Methods* **9**, 676–682 (2012).

10. Biomedical Imaging Group, MosaicJ, an ImageJ plugin for the creation of an image mosaic, *École polytechnique fédérale de Lausanne (EPFL)* (2025). https://bigwww.epfl.ch/thevenaz/mosaicj/.

11. M. D. Abramoff, P. J. Magalhães, S. J. Ram, Image Processing with ImageJ. *Biophotonics international* **11**, 36–42 (2004).

12. P.-C. Bürkner, brms: An R Package for Bayesian Multilevel Models Using Stan. *Journal of Statistical Software* **80**, 1–28 (2017).

13. D. Bates, M. Mächler, B. Bolker, S. Walker, Fitting Linear Mixed-Effects Models using lme4. *arXiv:1406.5823*, doi: https://doi.org/10.48550/arXiv.1406.5823 (2014).

14. R. V. Lenth, emmeans: Estimated Marginal Means, aka Least-Squares Means, (2017); https://doi.org/10.32614/CRAN.package.emmeans.

15. R Core Team, R: A language and environment for statistical computing, (2020); https://www.R-project.org/.